RSC Advances

PAPER

View Article Online
View Journal | View Issue

Cite this: *RSC Adv.*, 2021, **11**, 36007

Effect of Ce doping on the structure–activity relationship of $MoVO_x$ composite metal oxides†

Luyao Deng,[a] Shuangming Li,*[ab] Yongwei Liu,[a] Zixuan Lu,[a] Yaoxin Fan,[a] Yunong Yan[a] and Sansan Yu *[ab]

A series of Ce-doped $MoVO_x$ composite metal oxide catalysts were prepared by the rotary evaporation method. The effects of Ce doping ratio on the crystal phase composition, morphology and surface properties of the catalysts were investigated. The results show that the crystal phase composition of samples with different Ce doping content is also obviously different. When the doping amount is small, $V_{0.95}Mo_{0.97}O_5$ is the main crystal phase, while MoO_3 is dominant when the doping amount is large. The Ce-doped catalyst showed obvious rod-shaped morphology and its average single point pore diameter and the number of acidic sites increased. Compared to the un-doped $MoVO_x$, the pore size of the sample synthesized at a Mo/Ce atomic ratio of 10/1 exhibited an increase of 41.11 nm. In addition, the effect of Ce doping on the catalytic performance of $MoVO_x$ was investigated with the selective oxidation of benzyl alcohol as a probe reaction. After doping, the $MoVO_x$ catalyst showed improved benzyl alcohol conversion and selectivity to benzaldehyde. At a Mo/Ce atomic ratio of 10/1, the conversion rate of benzyl alcohol reaches 83.26%, which is 64.56% higher than that without doping, and the highest product yield can reach 76.47%.

Received 19th July 2021
Accepted 21st October 2021

DOI: 10.1039/d1ra05531c

rsc.li/rsc-advances

1. Introduction

The selective oxidation of alcohols and hydrocarbons is one of the important reactions in the chemical industry. Through this reaction, a series of high value-added oxygen-containing products such as alcohols, aldehydes, ketones, and acids can be produced.[1–3] The selective oxidative dehydrogenation of benzaldehyde is a typical example. However, the type of catalyst has an important influence on the formation of the target product. In the past few years, the most commonly used catalysts for selective oxidation of benzyl alcohol are heterogeneous catalysts, and metal-based oxides are some of the most important heterogeneous catalysts.[4–7] Among them Mo based oxides have broad prospects in the selective oxidation of alcohols and hydrocarbons due to their unique structure and catalytic performance. At present, Mo–V–O composite metal oxides are widely used in selective oxidation of alcohols and hydrocarbons, such as oxidation of glycerol to acrylic acid, and oxidation of propane, acrolein, and isobutane to acrylic acid, and ethane, respectively.[8–10] Studies have shown that the single metal oxide MoO_3 can exhibit excellent catalytic activity in alcohol dehydrogenation reactions, but MoO_3 alone is prone to phase change and deactivation during the catalytic process.[11,12] When MoO_3 and other Mo based oxides co-exist, they can form a synergistic effect with the main crystalline phase, which can significantly improve the selectivity of the catalyst and prolong the service life of the catalyst. However, it is still difficult for the catalytic performance of Mo–V–O composite metal oxides to meet the needs of industrialization. How to further improve its catalytic performance (*i.e.* raw material conversion and product selectivity) is an urgent problem to be solved in this field. It is documented that the structure of $MoVO_x$ is the decisive factor affecting its catalytic performance, in which the crystal phase composition, pore size, and redox capacity are affected by the preparation conditions.[13–16] Therefore, the structure of the catalyst can be optimized by controlling the preparation method and conditions.

At present, the methods for optimizing catalyst structure mainly include carrier supporting, weak acid treating, additives adding and element doping.[17–19] Among them, as a simplest and effective method, element doping has been widely used in the improvement of composite metal oxide catalysts structure and properties in recent years.[20] For example, introduce a less amount of W element can enhance the acidity of Mo–V–O catalyst, and the yield of glycerol oxidation to acrylic acid can reaches 50.5%, the doping of P doping can increase the acidic sites of the Mo–V–Te–O catalyst and increase the selectivity of propane oxidation to acrylic acid, from almost zero to 17%.[17]

[a]*College of Chemical Engineering, Shenyang University of Chemical Technology, No. 9, 11 St., Shenyang Economic & Technological Development Zone, Shenyang 110142, China. E-mail: lishuangming@syuct.edu.cn*

[b]*Key Laboratory of Chemical Separation Technology of Liaoning Province, Shenyang University of Chemical Technology, Shenyang 110142, China. E-mail: ssyu@syuct.edu.cn; Fax: +86 24 89383760; Tel: +86 24 89388453*

† Electronic supplementary information (ESI) available. See DOI: 10.1039/d1ra05531c

The addition of Au can change the particle morphology of Mo–V–Te–Nb–O catalyst and significantly promote the oxidative dehydrogenation of propane.[21] Mn can enhance the surficial V^{5+} content of Mo–V–Te–Nb–O catalyst, improving the catalytic performance of the catalyst for oxidative dehydrogenation of ethane to ethylene.[22] Mg doping can improve the activity of Mo–V–W–Cu–Sb catalyst, in which the conversion rate of acrolein and the yield of acrylic acid reaches 99.2% and 95.2%, respectively.[18] The appropriate amount of Cr doping can reduce the strength of acidic sites of Mo–V–Te–Nb–O catalyst, promoting the activation of propane and the selectivity (78.3%).[23] In addition, the rare earth element cerium (Ce) is also an important element for the structural optimization of composite metal oxides. The existence of Ce will affect the growth process of catalyst particles, which is conducive to obtain small-size particles.[24] Moreover, due to the Ce element has unique redox properties and high oxygen storage capacity, the Ce^{3+}/Ce^{4+} ion pair formed on the surface of the composite metal oxide can significantly increase the redox capacity of the catalyst, enhancing the migration of lattice oxygen and the catalytic activity of oxides.[25]

To our knowledge, there is no report on the effect of Ce doping on the structure and performance of Mo–V–O composite metal oxide catalyst at present. In this work, the effect of Ce doping amount on the crystal phase composition, specific surface area, pore size, particle size, acidic sites, and morphology of $MoVO_x$ is investigated. Furthermore, the catalytic performance of Ce-doped $MoVO_x$ in the selective oxidation of benzyl alcohol to benzaldehyde is also studied. An appropriate Ce doping ratio can change the crystal phase structure and micromorphology of the catalyst and improve the catalytic performance, in which the conversion rate of benzyl alcohol and the selectivity of benzaldehyde reached 83.26% and 91.81%, respectively.

2. Experimental section

2.1 Preparation

Ce-doped $MoVO_x$ composite metal oxide catalysts were prepared by the rotary evaporation method. Weigh $(NH_4)_6Mo_7O_{24}\cdot 4H_2O$, NH_4VO_3 and $Ce(NO_3)_3\cdot 6H_2O$ according to Mo/V/Ce (molar ratio) = $1 : 0.4 : x$ (x = 0, 0.02, 0.05, 0.10, 0.20, 0.33) and dissolve them in 100 mL deionized water to obtain mixed solution A, which was stirred at a constant temperature of 70 °C for 30 minutes, obtaining a clear and transparent orange-yellow solution B, the solution B was rotary evaporated and then precursor was obtained. The precursor was calcined in air at 260 °C for 2 h, and then calcined in nitrogen at 500 °C for 2 h. Ce doped $MoVO_x$ was obtained. The catalyst particles with a diameter of 0.90–0.45 mm were obtained by grinding, tableting, crushing, and sieving. The preparation ratio of the Ce doped catalyst is shown in Table 1.

$(NH_4)_6Mo_7O_{24}\cdot 4H_2O$, NH_4VO_3, C_7H_8O, $Ce(NO_3)_3\cdot 6H_2O$ and C_7H_6O were analytical reagent (AR) grade and purchased from Sinopharm Chemical Reagent Co, Ltd. (Shanghai, China), C_7H_8, $C_8H_8O_2$, C_2H_6O, C_6H_{12} were analytical reagent (AR) grade and purchased from HengXing Chemical Reagent Co, Ltd. (Tianjin, China). Deionized water (H_2O) made in the laboratory.

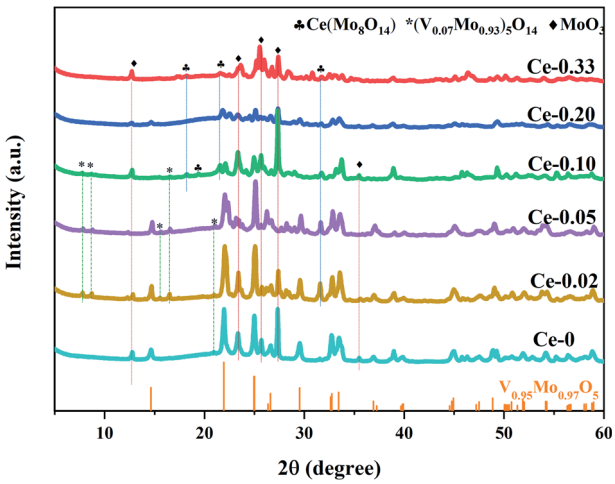

Fig. 1 The XRD patterns of $MoVO_x$ sample with different doping ratio of Ce.

2.2 Characterization

The structure and purity of the products were identified by XRD, which was carried out on a D8 Advance X-ray generator (Bruker AXS Company, Germany) by using Cu K_α radiation. The X-ray intensity was measured over a 2θ diffraction angle from 5° to 60° with a step size of 5° min^{-1}. Scanning electron microscopy (SEM) observations were performed on a field emission scanning electron microscope (Gimin300, ZEISS, Germany). The specific surface area was recorded by the BET method using nitrogen adsorption–desorption isotherms at liquid nitrogen temperature of −196 °C on an Autosorb-IQ gas adsorption

Table 1 Preparative composition of $MoVO_x$ catalysts with different doping mole ratio of Ce

Catalyst	Mo	V	Ce
Ce-0	1	0.4	0
Ce-0.02	1	0.4	0.02
Ce-0.05	1	0.4	0.05
Ce-0.10	1	0.4	0.1
Ce-0.20	1	0.4	0.2
Ce-0.33	1	0.4	0.33

Table 2 The specific surface area, average pore radius and average particle size of $MoVO_x$ catalysts doped with different content of Ce

Catalyst	S_{BET}[a] ($m^2\ g^{-1}$)	D_P[a] (nm)	Average grain size[b] (nm)
Ce-0	7.035	26.01	2699.92
Ce-0.02	5.391	47.80	2573.83
Ce-0.05	6.779	29.79	2523.08
Ce-0.10	4.828	67.12	2124.37
Ce-0.20	5.414	39.99	2062.57
Ce-0.33	4.458	31.55	1287.89

[a] Calculated by BET analysis. [b] Calculated from XRD data using Scherrer formula.

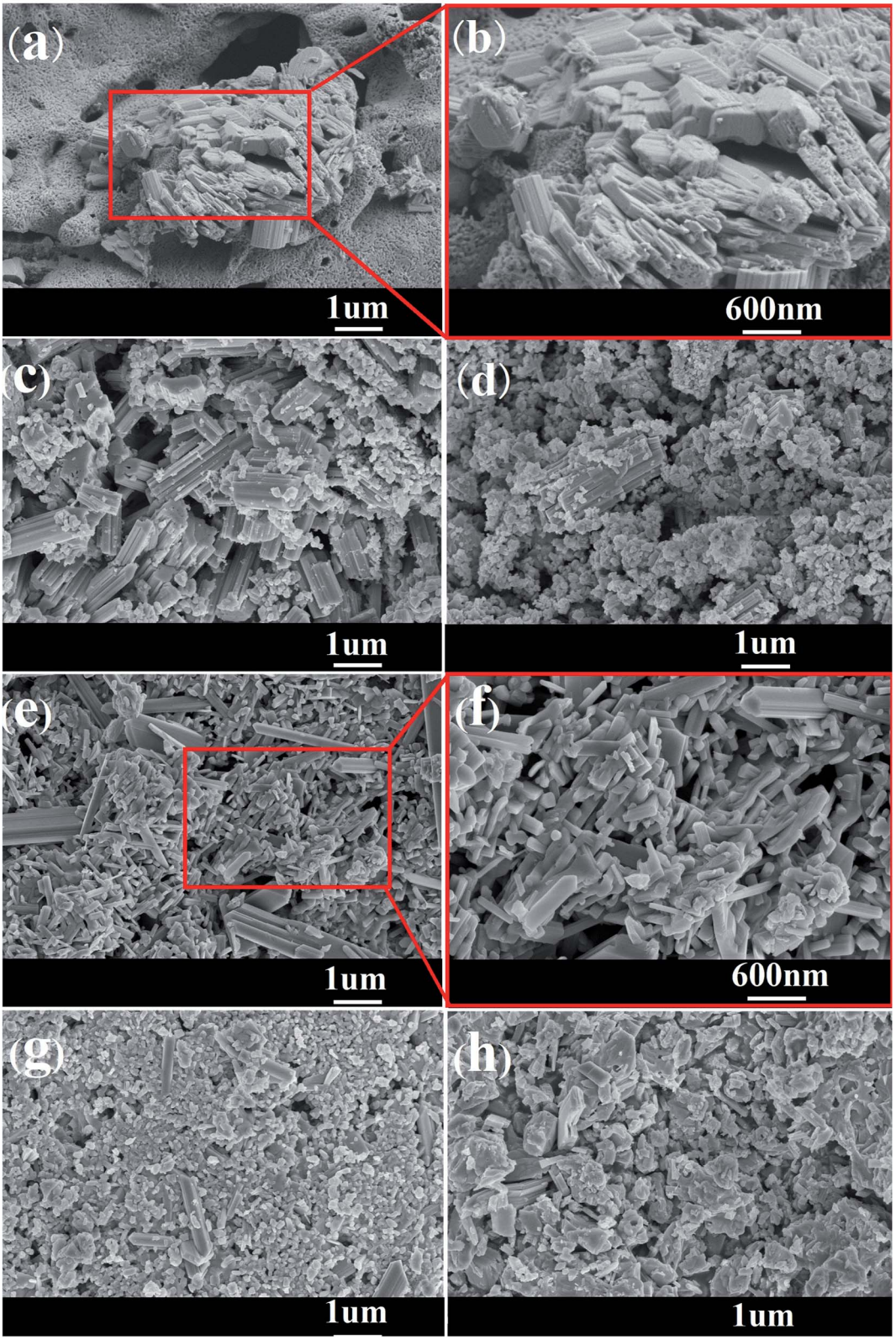

Fig. 2 The SEM images of $MoVO_x$ with different doping ratio of Ce. Ce-0 (a), local amplification of Ce-0 (b), Ce-0.02 (c), Ce-0.05 (d), Ce-0.10 (e), local amplification of Ce-0.10 (f), Ce-0.20 (g), Ce-0.33 (h).

analyzer (Beijing Builder, China). Hydrogen temperature-programmed reduction (H_2-TPR) and ammonia temperature-programmed desorption (NH_3-TPD) were carried out in a ChemBET system (Quantachrome, USA) equipped with a thermal conductivity detector. For H_2-TPR, 0.1 g catalyst was reduced in 10% H_2/Ar with a flow rate of 30 mL min^{-1} from

room temperature to 900 °C at a heating rate of 10 °C min^{-1}. For NH_3-TPD, catalysts were carried out in 7% NH_3/He from room temperature to 950 °C with the same heating rate. The X-ray photoelectron spectroscopy (XPS) was carried out on an ESCALAB 250Xi spectrometer (Thermo Fischer, USA), in which the excitation source was Al Kα ray ($h\nu$ = 1486.6 eV). All binding energies (BE) were calibrated by using C 1s peak of contaminant carbon (BE = 284.6 eV) as an internal standard.

2.3 Catalytic tests

The oxidation of benzyl alcohol was carried out in a fixed-bed stainless steel tubular reactor (i.d. 8 mm, length 400 mm). The carrier gas is a mixture of nitrogen and oxygen, reactor was heated to the reaction temperature. The raw material solution with a concentration of 50% was prepared by dissolving benzyl alcohol in cyclohexane. The raw material solution (0.05 mL min^{-1}) was supplied through a syringe pump. The raw steam is mixed with N_2 and O_2 and then enters the reactor. The space velocity is 30.87 h^{-1}. The reaction products were collected at a given time interval after being condensed with ice water and then analyzed by a liquid chromatograph (HPLC, Agilent 1260, USA) equipped with diode array (DAD) as detector and ZORBAX SB-C18 chromatography columns.

3. Results and discussion

3.1 Characterization

3.1.1 XRD. Fig. 1 shows the XRD patterns of $MoVO_x$ samples with different Ce doping contents. The XRD patterns of all samples were indexed to $V_{0.95}Mo_{0.97}O_5$ (PDF 77-0649) and MoO_3 (PDF 76-1003) crystal phases. In addition, for Ce-0, Ce-0.02, Ce-0.05 and Ce-0.10, these peaks at 2θ = 7.7, 8.6, 15.5, 16.4 and 20.9° indicate $(V_{0.07}Mo_{0.93})_5O_{14}$ (PDF 31-1437) also exists in these samples. For Ce-0.10, Ce-0.20 and Ce-0.33, another phase (2θ = 15.3, 19.2, 21.3 and 31.5°) corresponding to $Ce(Mo_8O_{14})$ (PDF 83-0636) emerges in the pattern. Compared to the un-doped $MoVO_x$ (Ce-0), the XRD patterns has obvious changes, the crystal phase composition of Ce-0.02 and Ce-0.05 with less Ce doping content is basically identical to that of un-doped Ce-0, and there is no obvious difference in the intensity of different diffraction peaks. The diffraction peaks intensity of $V_{0.95}Mo_{0.97}O_5$ decreases with the increase of Ce doping ratio. The average grain size of each catalyst calculated by the Scherrer equation also decreases with the increase of Ce doping ratio (Table 2), which is due to the adsorption of cerium ions on the surface of the catalyst to inhibit the growth of crystal grains.[26]

3.1.2 SEM. Fig. 2 shows the SEM images of $MoVO_x$ with different Ce doping contents and the un-doped sample, the main morphology of all catalysts are rod-shaped and small particles. Fig. 2a and b show that un-doped $MoVO_x$, Ce-0 samples possessed the serious agglomeration of particles, the main morphology is layered lamellar formed by stacking several rod-shaped, therefore, there are fewer rod-shaped exposed alone, which affects the performance of the catalyst. However, with the doping of Ce, Fig. 2c and d show that the overall rod-shaped stackable morphology begins to disperse into rod-shaped clusters (Ce-0.02 and Ce-0.05). When the doping amount of Ce reaches the Mo/Ce atomic ratio of 10/1, the rod-shaped of $MoVO_x$ is completely dispersed (see Fig. 2e and f). However, with the further increase of Ce content, Ce-0.20

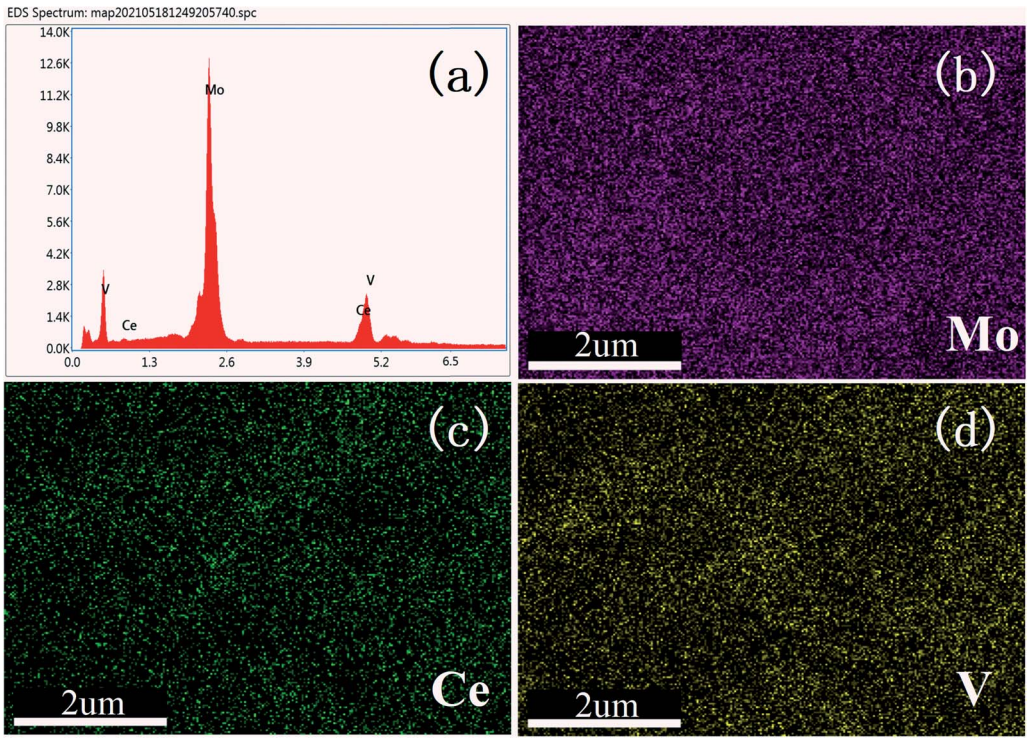

Fig. 3 EDX spectra (a) and EDX mapping images of Ce-0.10 catalyst (b–d).

sample mainly presents dispersed small particles with a diameter of approximate 100 nm (Fig. 2g). While Fig. 2g shows that Ce-0.33 sample, with the largest Ce doping content, presents large irregular grains. It can be seen from Fig. 2 that the dispersion of $MoVO_x$ particles can be significantly improved with appropriate Ce doping amount. However, excessive doping of Ce may destroy the original pore structure of the $MoVO_x$ catalyst, resulting in a significant decrease in the pore size of the $MoVO_x$ catalyst, Table 2 shows that the average pore radius of a single point decreased from 67.12 nm to 31.55 nm.

For further verification of the incorporation of Ce atoms, EDS elemental mapping images were obtained for the Ce-0.10 sample, as shown in Fig. 3. The results show that all components (Mo, V, and Ce) were highly distributed within the samples. There is no evidence of metal oxide aggregation or segregation effect. The highest content of Mo atom is 73%, V atom is 18%, and Ce atom is 9%.

3.1.3 BET. The N_2 adsorption–desorption isotherms and specific surface area and pore size of $MoVO_x$ catalysts with different Ce doping amounts are shown in Fig. 4. The results show that the isotherm profiles of all the samples exhibit a type III isotherm based on the IUPAC classification. With the increase of Ce doping, the specific surface area of the catalyst decreased from 7.035 to 4.458 $m^2\ g^{-1}$, indicating that the doping of Ce has a significant effect on the specific surface area of the catalyst. The single point average pore radius increases from 26.01 to 67.12 nm, and the Ce-0.10 sample shows the largest pore radius, the average grain size decreases with the increase of Ce doping, showing an obvious downward trend.

3.1.4 H_2-TPR. The reduction behaviors of $MoVO_x$ with different Ce doping contents are examined by H_2-TPR. As Fig. 5 shows, all catalysts mainly exhibits a reduction peak at around 750 °C, it has been reported that the peak at around 750 °C results from the Mo^{6+} to Mo^{4+} reductions, and the peak at around 675–725 °C is assigned to the reduction of V^{5+} to V^{3+},[27] the two hydrogen consumption peaks shift to a low temperature with the increase of Ce doping amount, indicating that the Ce doping can enhance activity center becomes more active and is easily reduced. With the increase of Ce doping, Ce-0.10 sample showed another reduction peak at 797 °C, this reduction peak results from the Ce^{4+} to Ce^{3+},[26] it is probably caused by $Ce(Mo_8O_{14})$ crystal phase. The reduction peak area of Ce-0.20 and Ce-0.33 increases obviously, which is consistent with the increase of $Ce(Mo_8O_{14})$ phase content in XRD, and the Ce-0.33 sample also formed a new high temperature reduction peak at 837 °C. According to the literature, the temperature of the reduction peak is related to the catalyst lattice oxygen,[28] after Ce doping, the temperature of the reduction peak shifts to low temperature, which indicates that the lattice oxygen reactivity of $MoVO_x$ is enhanced.

3.1.5 NH_3-TPD. The acid sites of as-synthesized samples were determined by NH_3-TPD and the profiles are presented in Fig. 6. There are only two NH_3 desorption peaks in un-doped Ce-0 samples, while the $MoVO_x$ catalyst with different Ce doping exhibit three main NH_3 desorption peaks, desorption peaks

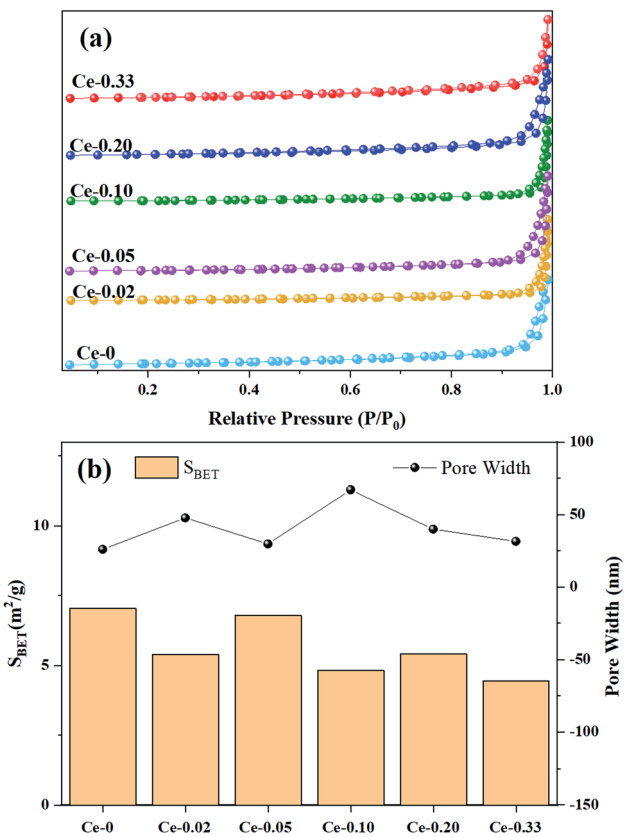

Fig. 4 Nitrogen adsorption–desorption isotherms. Specific surface area (column graph) (a) and pore size (line graph) (b).

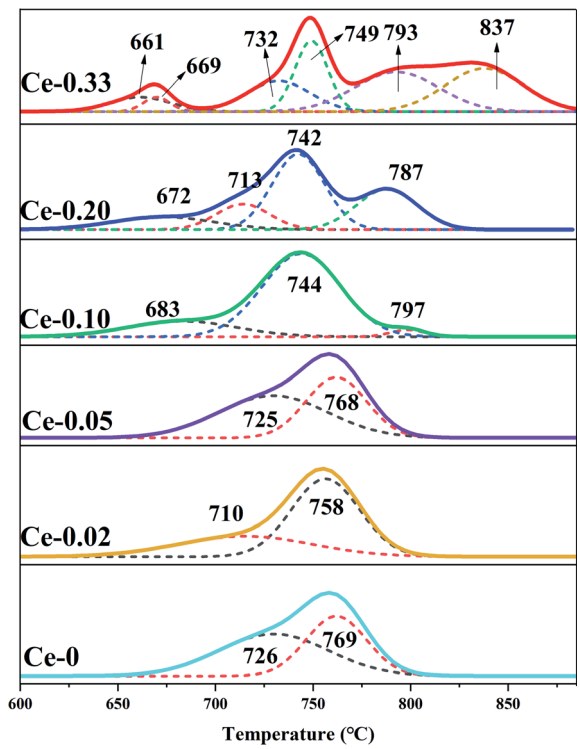

Fig. 5 The H_2-TPR profiles of $MoVO_x$ catalysts with different doping ratio of Ce.

appear after 275 °C, which belong to strong Brønsted acid sites.[29–31] With the increase of Ce doping, the desorption temperature first decreases and then increases. The Ce-0.05 and Ce-0.10 samples shows lower desorption temperature, the desorption peak area of Ce-0.10 is significantly larger than Ce-0.05, showing the lowest desorption temperature and the largest desorption peak area, indicating that Ce-0.10 contains more Brønsted acid sites.

3.1.6 XPS. Fig. 7a–e present the XPS survey spectrum and high resolution spectra of Mo 3d, V 2p, Ce 3d and O 1s, in which the adventitious C 1s peak at 284.6 eV was applied to calibrate the XPS spectra. According to the literature, the Mo $3d_{5/2}$ BE peak of Ce-doped $MoVO_x$ located at 232.65 eV indicate that the surface Mo species consist of Mo^{6+} (232.9 eV) and Mo^{5+} (232.0 eV), and the amount of Mo^{6+} outweighs that of Mo^{5+}. The peak centered at 516.4 eV correspond to V $2p_{3/2}$, between 517.0 eV (V^{5+}) and 516.0 eV (V^{4+}), confirming the existence of V^{5+} and V^{4+}, with V^{5+} dominating.[32–34] As shown in Fig. 7f, With the increase of V^{5+} content in Ce doped $MoVO_x$ samples, the ratio of V^{5+} to V $2p_{3/2}$ peak area increases from 65.87% to 86.88%, with the increase of the proportion of Mo^{6+} and V^{5+} to Mo 3d and V 2p respectively, Mo^{6+} and V^{5+} in $MoVO_x$ catalyst are easy to reduce and gradually shift to low temperature, which is consistent with the change of reduction peak at 750 °C and 675–625 °C in Fig. 5. The existence of Ce is confirmed in Fig. 7d, which shows that the spectrum of Ce is composed of eight peaks, they are respectively marked as α, α′, α″, α‴ and β, β′, β″, β‴, among which the peaks of α′ and β′ are attributed to Ce^{3+}, and α, α″, α‴, β, β″, β‴ are attributed to Ce^{4+}. As can be seen from Table 3, the addition of Ce had little effect on the contents of Mo 3d and V 2p in the $MoVO_x$ catalyst, while the content of Ce 3d was gradually increasing, and the contents of Ce-0, Ce-0.02, and Ce-0.10 were 0%, 0.92%, and 3.56%, respectively, the proportion of Ce^{4+} in Ce 3d decreases with the increase of Ce doping, from 65.03% to 64.12%, which is consistent with the increasing trend of the reduction peak area at 770–875 °C in Fig. 5. In Fig. 7e, at 530.5 eV and 531 eV correspond to lattice oxygen and oxygen vacancy, respectively,[35,36] Xu pointed out that Ce has superior oxygen storage capacity, which is conducive to the formation of unsaturated chemical bonds and oxygen vacancies,[37] the ratios of the O2 peak area to the total peak area of O1 and O2 in Ce-0, Ce-0.02 and Ce-0.10 are 61.25%, 65.27%, and 72.11%, respectively, indicating that the $MoVO_x$ catalyst has more oxygen vacancies after Ce doping.

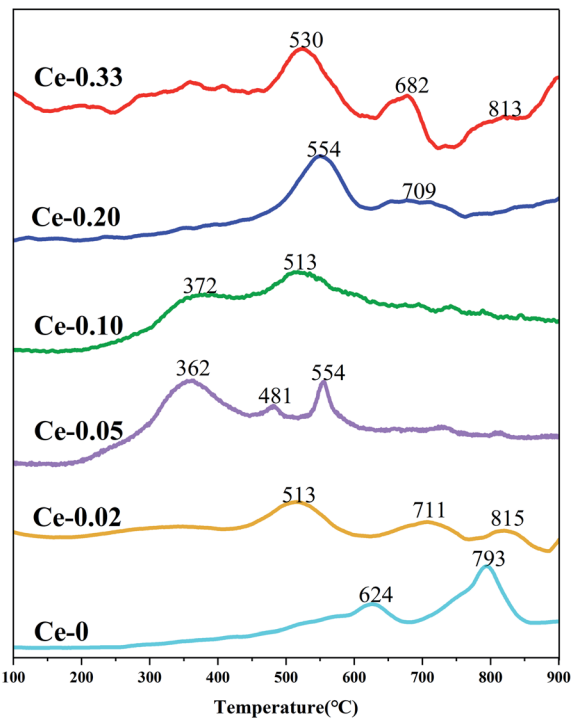

Fig. 6 The NH_3-TPD profiles of $MoVO_x$ catalysts with different doping ratio of Ce.

3.1.7 Catalytic performance. The catalytic performance of $MoVO_x$ with different Ce doping contents was tested for the selective oxidation of benzyl alcohol to benzaldehyde at different catalytic temperatures with an interval of 20 °C and the results are shown in Fig. 8. Fig. S1† shows all the HPLC chromatograms for the conversion of benzyl alcohol to benzaldehyde. It can be observed that different Ce doping contents have obvious effects on benzyl alcohol conversion, benzaldehyde selectivity, and yield. As shown in Fig. 8a, the difference in catalytic activity was more pronounced in the first three samples with less doping, the catalytic performance of the two samples of Ce doped is significantly higher than that of un-doped while increasing the conversion rate, the selectivity of the un-doped samples decreased the most, the slope of scattering trend line of Ce-0 conversion rate and selectivity is larger than that of other Ce doped samples. The conversion of Ce-0 is increased by 7.8% while the selectivity is decreased by 9.4%. The Ce doped sample is more stable, the conversion of Ce-0.10 sample is increased by 61%, and the selectivity is only decreased by 5.73%, the results indicate that Ce doping can greatly improve the catalytic activity of $MoVO_x$ catalyst. Fig. 8b shows that the yield of benzaldehyde is positively correlated with the reaction temperature. As the reaction temperature increases, the yield of benzaldehyde also gradually increases, the yield reaches a maximum of 76.47% at 320 °C for sample Ce-0.10, the yield of the first three samples with less Ce doping is not greatly affected by temperature, it may be related to their similar crystal phase structure. When the reaction temperature is increased, and the doping amount of the Ce element is increased, the catalytic performance begins to decrease, but it is still better than the first three samples.

With the doping of Ce, the crystal phases of $V_{0.95}Mo_{0.97}O_5$ and $(V_{0.07}Mo_{0.93})_5O_{14}$ gradually disappear, and $Ce(Mo_8O_{14})$ gradually forms; in Ce-0.10 samples, MoO_3 has the highest diffraction peak intensity, and its synergistic effect with $V_{0.95}Mo_{0.97}O_5$ is also the most significant. The specific surface area of the catalyst is similar and does not change much. There is a rising first and falling trend in pore diameter, the grain size gradually becomes smaller, the reduction temperature shifts to low temperature. However, for the three samples with more Ce doping, the Ce^{4+} content decreased, the reduction peak area corresponding to the Ce element increased, and a new high-temperature reduction peak appeared, this probably one of the reasons that the performance of Ce-0.10 samples have been

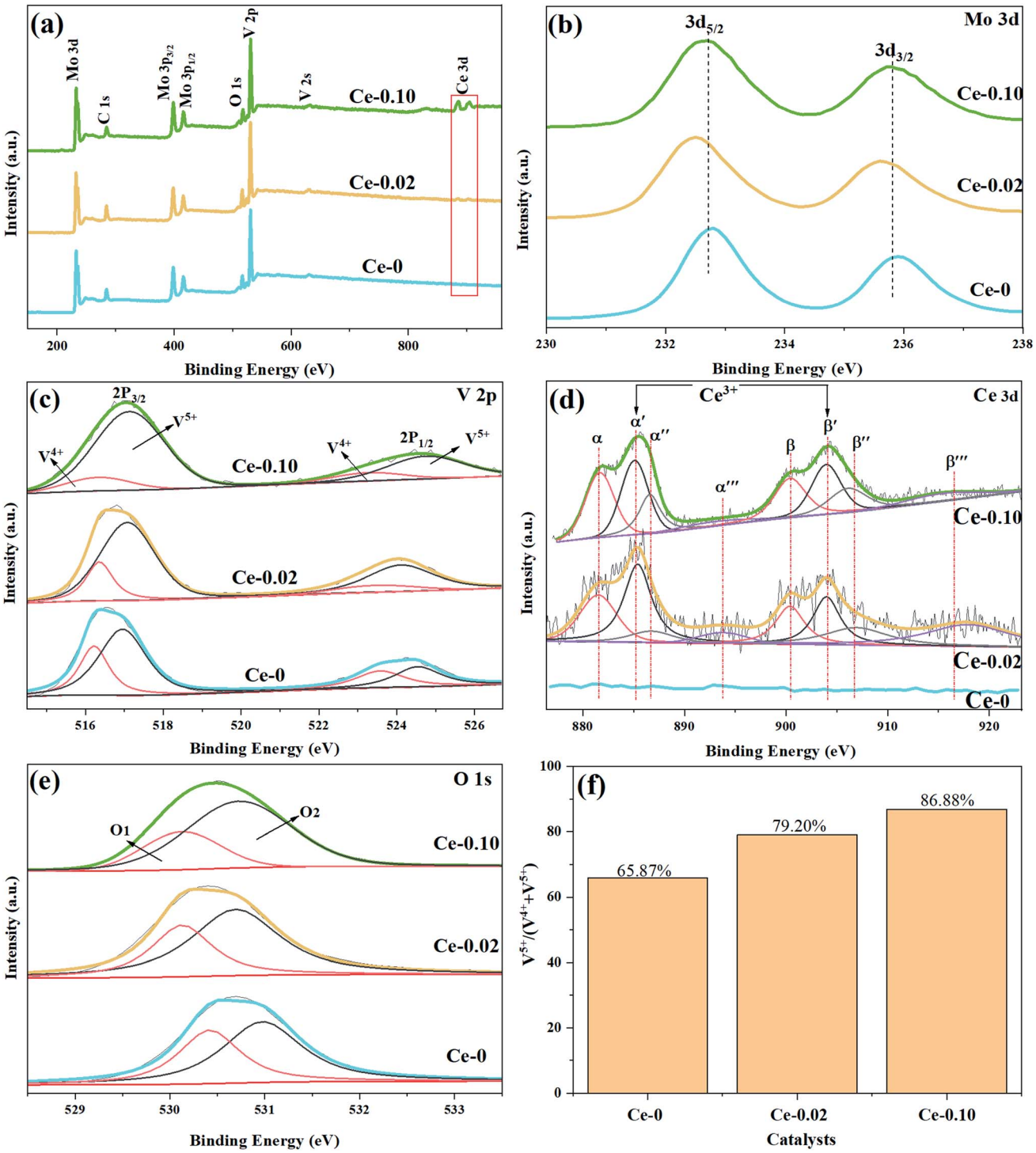

Fig. 7 XPS survey spectrum of Ce doped $MoVO_x$ catalysts (a), high resolution spectra of Mo 3d (b), V 2p (c), Ce 3d (d), O 1s (e) and $V^{5+}/(V^{4+}+V^{5+})$ (f).

significantly improved, while the performance of Ce-0.20 and Ce-0.33 samples have been reduced. The Ce-doped catalyst contains more Brønsted acid sites, the trend of catalytic performance of different Ce doped $MoVO_x$ samples, was completely consistent with that of the changing trend of Brønsted acid sites. The best catalytic performance is achieved under the doping amount of the Ce-0.10 sample. At this time, the conversion of benzyl alcohol is 83.26%, the selectivity of benzaldehyde is 91.81%, and the yield of benzaldehyde is 76.47%. Indicating that the amount of Ce doping is related to the NH_3 adsorption capacity, which has an important influence on the catalytic activity. With the increase of Ce doping ratio, the contents of Mo^{6+} and V^{5+} also increase, and the Ce 3d in the catalyst increased from 0.92% (Ce-0.02) to 3.56% (Ce-0.10)

Table 3 The atom compositions of $MoVO_x$ catalysts with different doping ratio of Ce

	Atomic (%)		
Catalyst	Ce 3d	Mo 3d	V 2p
Ce-0	0	34.20	10.87
Ce-0.02	0.92	27.48	11.56
Ce-0.10	3.56	32.42	10.86

(Table 3). Ce doping makes the catalyst pore size larger and greatly improves the oxygen storage capacity. At the same time, the rod-shaped is fully exposed, resulting in the increase of active sites in contact with raw materials, and the lower reduction temperature is more conducive to the improvement of catalytic performance. The results show that the performance of the $MoVO_x$ catalyst is greatly improved by doping Ce, but excessive Ce doping will have a negative effect on the catalytic performance.

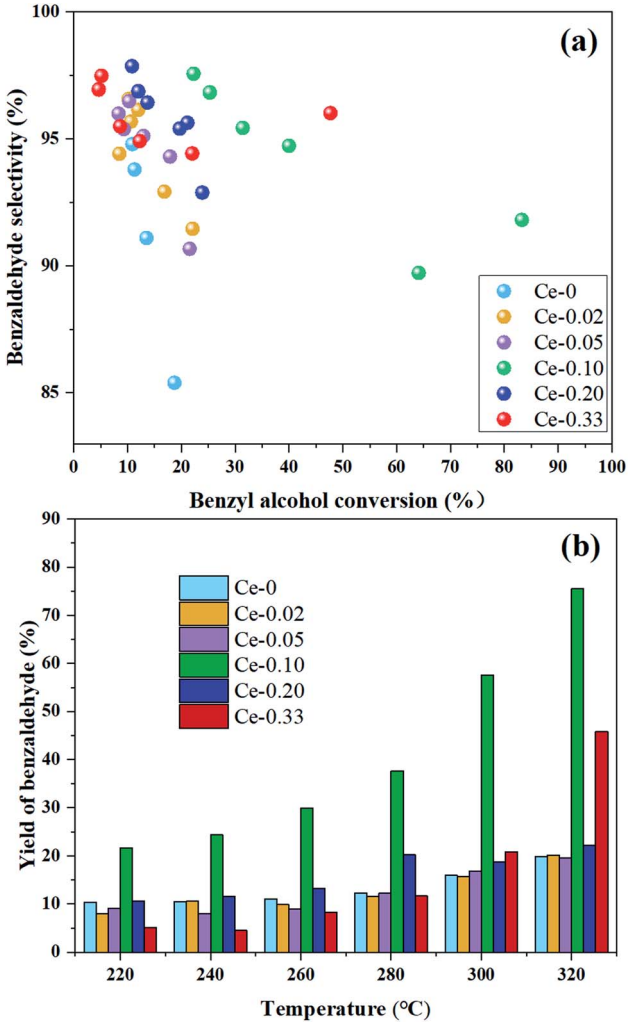

Fig. 8 The catalytic performance of $MoVO_x$ catalysts with different doping ratio of Ce. Trend of benzyl alcohol conversion and benzaldehyde selectivity (a), relationship between yield of benzaldehyde and reaction temperature (b).

4. Conclusions

Six Ce-doped $MoVO_x$ composite metal oxides were fabricated by using the rotary evaporation method and their catalytic performance was investigated. It is concluded that the crystalline phase, morphology, surface properties, as well as acidic and redox properties were influenced greatly by the Ce doping. The addition of Ce in $MoVO_x$ can improve the reducibility at low temperature, increase the average pore size and the number of acid sites, and improves the aggregation of rod-shaped, enhances the activity of lattice oxygen reaction, and significantly improves the catalytic performance of $MoVO_x$. $MoVO_x$ prepared with Mo/Ce atomic ratio of 10/1 exhibits the best catalytic performance due to its largest pore size, the most acidic sites, and well-dispersed rod-shaped morphology, in which the benzyl alcohol conversion and selectivity to benzaldehyde achieved 83.26% and 91.81%, respectively.

Conflicts of interest

There are no conflicts to declare.

Acknowledgements

The authors gratefully acknowledge the financial supports by the National Natural Science Foundation of China (No. 21706165), Scientific Research Fund of Liaoning Provincial Education Department, China (No. LQ2019007) and LiaoNing Revitalization Talents Program (No. XLYC2002001), and Natural Science Foundation of Liaoning Province, China (No. 2021-MS-255).

References

1 C.-G. Gamaliel, Q.-S. Roberto, S. R.-M. Richard, J. S. Valente and O. C.-A. Carlos, *Chem. Eng. J.*, 2014, **252**, 75–88.
2 D. Delgado, R. Sanchís, J. A. Cecilia, E. Rodríguez-Castellón, A. Caballero, B. Solsona and J. M. López Nieto, *Catal. Today*, 2019, **333**, 10–16.
3 G. Reena, S. Bipul, B. Arijit, L. Frederic, S. Siddharth, P. Chandrashekar and B. Ankur, *J. Mater. Chem. A*, 2016, **4**(47), 18559–18569.
4 K. Y. Koltunov, E. V. Ishchenko and V. I. Sobolev, *Catal. Commun.*, 2018, **117**, 49–52.
5 D. P. Cristina, F. Ermelinda and R. Michele, *J. Catal.*, 2008, **260**(2), 384–386.
6 Z. Wang, J. J. Feng, X. L. Li, R. Oh, D. D. Shi and O. Akdim, *J. Colloid Interface Sci.*, 2021, **588**, 787–794.
7 L. L. Li, X. J. Zhou, L. Liu, S. Jiang, Y. J. Li and L. X. Guo, *Catalysis*, 2019, **9**(6), 538.
8 M. O. Guerrero-Pérez, M. C. Herrera, I. Malpartida, M. A. Larrubia and L. J. Alemany, *Catal. Today*, 2006, **118**(3–4), 360–365.

9 X. C. Zhang, M. Wang, C. F. Zhang, J. M. Lu, Y. H. Wang and F. Wang, *RSC Adv.*, 2016, **6**(75), 70842–70847.
10 L. F. Rasteiro, L. H. Vieira, C. V. Santilli and L. Martins, *RSC Adv.*, 2018, **8**(22), 11975–11982.
11 K. V. Raun, L. F. Lundegaard, B. Pablo, C. C. Appel, N. Kenneth, T. Max, S. Max, D. J. Anker, D. G. Jan and H. Martin, *Catal. Lett.*, 2019, **150**, 1434–1444.
12 Y. M. He, Y. Wu, W. Z. Weng and H. L. Wan, *J. Nat. Gas Chem.*, 2011, **20**(3), 249–255.
13 Z. X. Yu, W. Zheng, W. L. Xu, P. Zhang, H. Y. Fu and Y. H. Zhang, *T. Nonferr. Metal Soc.*, 2011, **21**, s405–s411.
14 B. M. Bacaa, A. Pigamoa, J. L. Duboisb and J. M. M. Millet, *Top. Catal.*, 2003, **23**(1), 39–46.
15 Q. He, J. Woo, A. Belianinov, V. V. Guliants and A. Y. Borisevich, *ACS Nano*, 2015, **9**(4), 3470–3478.
16 B. Z. Chu, L. Truter, T. A. Nijhuis and Y. Cheng, *Appl. Catal. Gen.*, 2015, **498**, 99–106.
17 R. K. Grasselli, C. G. Lugmair, A. F. Volpe Jr, A. Andersson and J. D. Burrington, *Catal. Today*, 2010, **157**(1–4), 33–38.
18 X. J. Bian, *Studies on the selective oxidation of acrolein to acrylic acid over the Mo–V-based complex metal oxide catalysts*, Master's thesis, Hunan University, Changsha, 2014.
19 F. Wang and W. Ueda, *Appl. Catal. Gen.*, 2008, **346**(1–2), 155–163.
20 B. Deniau, J. Millet, S. Loridant, N. Christin and J. L. Dubois, *J. Catal.*, 2008, **260**(1), 30–36.
21 E. V. Lazareva, V. M. Bondareva, D. A. Svintsitskiy, A. V. Ishchenko, A. S. Marchuk, E. P. Kovalev and T. Y. Kardash, *Catal. Today*, 2021, **361**, 50–56.
22 X. Chen, D. Dang, H. An, B. Chu and Y. Cheng, *J. Taiwan Inst. Chem. Eng.*, 2019, **95**, 103–111.
23 A. X. Xu, Y. Wang, H. Q. Ge, S. Chen, Y. H. Li and W. M. Lu, *Chin. J. Catal.*, 2013, **34**(12), 2183–2191.
24 J. Wen, H. Guo, X. Ma, Z. Wei, X. He, L. Zhang, B. Li, T. Wang and Y. Cheng, *Catal. Sci. Technol.*, 2020, **10**(11), 3739–3747.
25 X. Liu, S. Jiang, M. Niu, S. Li, W. Li and S. Yu, *J. Nanosci. Nanotechnol.*, 2019, **19**(2), 833–838.
26 X. Zhang, H. L. Wan, W. Z. Weng and X. D. Yi, *Catal. Lett.*, 2003, **87**, 3–4.
27 S. M. Li, H. Shao, L. L. Xu, C. Chen, J. S. Ma, Q. Liu, X. G. San, W. X. Li, N. Tsubaki and S. S. Yu, *J. Mol. Catal.*, 2014, **28**(2), 132–139.
28 H. Wang, Z. Deng, W. Chu and W. Yang, *React. Kinet. Catal. Lett.*, 2009, **97**(2), 233–241.
29 D. Verma, B. S. Rana, R. Kumar, M. G. Sibi and A. K. Sinha, *Appl. Catal. Gen.*, 2015, **490**, 108–116.
30 D. Verma, R. Insyani, Y. W. Suh, S. M. Kim, S. K. Kim and J. Kim, *Green Chem.*, 2017, **19**(8), 1969–1982.
31 V. Ranaware, D. Verma, R. Insyani, A. Riaz, S. M. Kim and J. Kim, *Green Chem.*, 2019, **21**(5), 1021–1042.
32 K. Asakura, K. Nakatani, T. Kubota and Y. Iwasawa, *J. Catal.*, 2000, **194**(2), 309–317.
33 J. B. Wagner, O. Timpe, F. A. Hamid, A. Trunschke, U. Wild, S. S. Dang, R. K. Widi, S. Hamid and R. Schlögl, *Top. Catal.*, 2006, **38**(1–3), 51–58.
34 M. O. Guerrero-Pérez, M. C. Herrera, I. Malpartida, M. A. Larrubia and L. J. Alemany, *Catal. Today*, 2008, **133–135**, 919–924.
35 N. Hayashi, Y. Sakai, H. Tsunoyama and A. Nakajima, *Langmuir*, 2014, **30**(34), 10539–10547.
36 D. X. Yin, H. Yang, S. Wang, Z. D. Yang, Q. Y. Liu, X. X. Zhang and X. Zhang, *Colloid. Surface. Physicochem. Eng. Aspect.*, 2020, 607.
37 W. Xu, H. He and Y. Yu, *J. Phys. Chem. C*, 2009, **113**(11), 4426–4432.